Physical properties of $GdFe_2(Al_xZn_{1-x})_{20}$

N. Ni,* S. Jia,* G. D. Samolyuk,† A. Kracher, A. S. Sefat,† S. L. Bud'ko, and P. C. Canfield
Ames Laboratory and Department of Physics and Astronomy, Iowa State University, Ames, Iowa 50011, USA
(Received 18 October 2010; revised manuscript received 7 January 2011; published 15 February 2011)

The high ferromagnetic ordering temperature of the dilute, rare-earth-bearing, intermetallic compound $GdFe_2Zn_{20}$ has been understood as being the consequence of the Gd^{3+} moment being embedded in a nearly ferromagnetic Fermi liquid. To test this understanding in detail, single crystals of the pseudoternary series $GdFe_2(Al_xZn_{1-x})_{20}$ ($x \leqslant 0.122$) and $YFe_2(Al_xZn_{1-x})_{20}$ ($x \leqslant 0.121$) were grown out of Zn-rich solution. Magnetization, heat capacity, and resistivity measurements show that, with Al doping, the ferromagnetic phase transition temperatures of the $GdFe_2(Al_xZn_{1-x})_{20}$ compounds decrease from 86 K ($x = 0$) to 10 K ($x = 0.122$); for the nonmagnetic analog, the $YFe_2(Al_xZn_{1-x})_{20}$ series, the Stoner enhancement factor Z decreases from 0.88 ($x = 0$) to 0.35 ($x = 0.121$) in a similar manner. Tight-binding linear-muffin-tin orbital atomic-sphere approximation band structure calculations are used to rationalize this trend. These results, together with the earlier studies of the $R(Fe_{1-x}Co_x)_2Zn_{20}$ (R = Gd and Y) series, clearly highlight the importance of band filling and the applicability of even a simple, rigid-band model to these compounds.

DOI: 10.1103/PhysRevB.83.054416 PACS number(s): 75.10.Lp, 75.30.−m, 75.20.Hr, 75.50.Cc

I. INTRODUCTION

The study of strongly correlated electron systems has been one of the primary research focuses in condensed matter physics for decades. Of specific interest, intermetallic compounds in the vicinity of the Stoner limit[1] exhibit exotic magnetic properties, such as nearly or weakly ferromagnetic Fermi liquid behavior, due to their strongly correlated d electrons. Particular attention has been paid to those systems containing both $4f$ local moments and highly correlated conduction electrons due to the rich phases that result from the interactions between $4f$ and d electrons; among such materials, the RFe_2Zn_{20} compounds, which belong to the large RT_2Zn_{20} (R = rare-earth elements, Y, and U; T = Fe, Co, Ni, Ru, Rh, Os, Ir, and Pt) series,[2–7] provide an ideal experimental platform, not only because they show various magnetic properties but also because they can be easily substituted on a number of unique crystallographic sites.[3,4,8–10] RT_2Zn_{20} crystallizes in the $Fd\bar{3}m$ space group; the nearest and next-nearest neighbors of R and T atoms are all Zn. The R and T ions occupy their own unique crystallographic sites, $8a$ and $16d$, respectively. Zn occupies three different crystallographic sites, $96g$ (Zn1 site), $48f$ (Zn2 site), and $16c$ (Zn3 site). The RT_2Zn_{20} series manifests many interesting magnetic properties: $YbFe_2Zn_{20}$, together with the other five YbT_2Zn_{20} (T = Ru, Os, Co, Rh, and Ir) compounds, shows heavy-fermion behavior;[4,11–16] YFe_2Zn_{20} and $LuFe_2Zn_{20}$ are nearly ferromagnetic Fermi liquids (NFFLs);[3,8–10] RFe_2Zn_{20} (R = Nd, Sm, and Gd–Lu) compounds undergo ferromagnetic phase transitions and have different degrees of sensitivity to the structural disorder.[10,17] Doping studies have been performed on $GdFe_2Zn_{20}$ since it has an abnormally high T_c, at 86 K, for a compound with less than 5% atomic Gd inside the lattice:[3] by substituting Co for Fe, it was found that $Y(Fe_{1-x}Co_x)_2Zn_{20}$ can be tuned from a NFFL, YFe_2Zn_{20}, to a noncorrelated, paramagnetic, YCo_2Zn_{20} and $Gd(Fe_{1-x}Co_x)_2Zn_{20}$ can be tuned from ferromagnetic $GdFe_2Zn_{20}$ with T_c about 86 K to antiferromagnetic $GdCo_2Zn_{20}$ with T_N about 5.7 K in a similar fashion.[3] This study revealed that the high T_c in $GdFe_2Zn_{20}$, or in other words, the strong Ruderman-Kittel-Kasuya-Yosida interaction, is a consequence of embedding the large Gd^{3+} moment into the highly polarizable YFe_2Zn_{20} matrix which contributes a large density of conduction electrons at the Fermi level. However, in this study, the transition metal sites were directly perturbed by the substitution. Here, we report another way to tune the system without directly substituting at the transition metal site. Single crystals of $GdFe_2(Al_xZn_{1-x})_{20}$ ($x \leqslant 0.122$) and $YFe_2(Al_xZn_{1-x})_{20}$ ($x \leqslant 0.121$) were grown and characterized by magnetization, resistivity, and heat capacity measurements. We found a close relation between the decrease of T_c in the $GdFe_2(Al_xZn_{1-x})_{20}$ series and the reduction of the Stoner enhancement factor in the $YFe_2(Al_xZn_{1-x})_{20}$ series. The density of states of $YFe_2(Al_xZn_{1-x})_{20}$ ($x \leqslant 0.121$) was calculated by the tight-binding (TB) linear-muffin-tin orbital (LMTO) atomic-sphere approximation method and used to further understand this trend. These results, together with the earlier studies of $Gd(Fe_{1-x}Co_x)_2Zn_{20}$ and $Y(Fe_{1-x}Co_x)_2Zn_{20}$, clearly indicate the importance of even a simple band filling and the applicability of the rigid-band approximation to these chemically complicated compounds.

II. EXPERIMENTAL METHODS

Single crystals of $GdFe_2(Al_xZn_{1-x})_{20}$ and $YFe_2(Al_xZn_{1-x})_{20}$ were grown out of high-temperature, pseudoternary, solutions rich in Zn.[3,18] Gd or Y pieces, Fe pieces, Al shot, and Zn shot were mixed together according to the ratio $R : Fe : Al : Zn = 2 : 4 : 94x : 94(1 - x)$. Each mixture was loaded into a 2 ml alumina crucible and placed into a quartz tube; then an appropriate amount of quartz wool was added on top of the alumina crucible, and the quartz tube was sealed under a partial atmosphere (1/3) of Ar gas. The sealed quartz tube was heated up to 1000 °C over 3 h and held at 1000 °C for another 3 h. The growth was then cooled to 600 °C over 85 h. The excess liquid was decanted off the crystals at 600 °C by use of a centrifuge. All compounds were synthesized using the same procedure to minimize the possible variations in the structure disorder. 0.5% HCl acid was used to remove residual flux and oxide slag from the

crystal surfaces. As x increased, more nucleation sites were formed and the sample size became smaller. The dimensions decreased from $7 \times 7 \times 7$ mm^3 ($x = 0$) to $2 \times 2 \times 0.5$ mm^3 ($x = 0.122$).

Elemental analysis of all the samples was performed using wavelength-dispersive x-ray spectroscopy (WDS) in the electron probe microanalyzer of a JEOL JXA-8200 electron microprobe. The average x values, measured at several locations of the sample, x_{WDS}, will be used to identify all the compounds rather than the nominal concentration, x_{nominal}.

Room-temperature powder x-ray diffraction measurements, with a Si standard, were performed using a Huber 670 Guinier camera equipped with an area detector with Cu $K\alpha$ ($\lambda \sim 1.5406$ Å) radiation. Diffraction patterns were taken on ground single crystals from each batch. No detectable impurities were found in these compounds. The unit cell parameters were refined with unitcell software.[19] Error bars were taken as twice the standard deviation σ, which was obtained from the refinements by the UNITCELL software.

Single-crystal x-ray diffraction measurements were performed on the $GdFe_2(Al_xZn_{1-x})_{20}$ ($x = 0.017$) compound using a STOE image plate diffractometer with Mo $K\alpha$ radiation ($\lambda \sim 0.7093$ Å). The data were adjusted for Lorentz and polarization effects, and a numerical absorption correction was performed. The structural solutions were refined by full-matrix least-squares refinement using the Bruker shelxtl 6.1 software package. The atomic disorder in the crystals was checked by refining site occupancies.

DC magnetization $M(H)$ and $M(T)$, along the [111] direction for all compounds, were measured in a Quantum Design (QD) Magnetic Properties Measurement System (MPMS) superconducting quantum interference device magnetometer. $M(H)$ measurements were carried out from 0 to 55 kOe at 1.85 and 300 K for each sample (Fig. 1). The slight nonlinearity of $M(H)$ curves around 3 kOe at 300 K for $YFe_2(Al_xZn_{1-x})_{20}$ samples indicates the low level of ferromagnetic impurities; for $YFe_2(Al_xZn_{1-x})_{20}$ compounds, $M(T)$ measurements were carried out at 10 and 50 kOe from 1.85 K to 350 K. Susceptibilities were calculated as $\Delta M/\Delta H = [M(50\ \mathrm{kOe}) - M(10\ \mathrm{kOe})]/40$ kOe to eliminate the effect of these ferromagnetic impurities in these samples. For $GdFe_2(Al_xZn_{1-x})_{20}$ compounds, due to the significantly higher susceptibility, no contribution from ferromagnetic impurities can be detected. Since high fields can shift and broaden the features of ferromagnetism, $M(T)$ measurements were carried out at 1 kOe from 1.85 to 350 K; susceptibilities were calculated as $\chi = M(T)/H$.

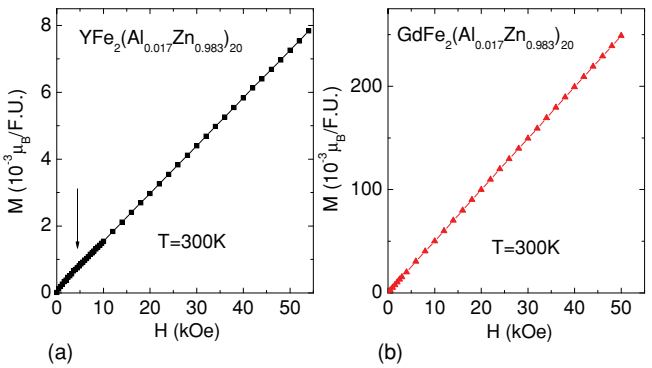

FIG. 1. (Color online) Room-temperature $M(H)$. The arrow draws attention to the slight nonlinearity of the $M(H)$ curve at room temperature.

AC transport measurements were performed using the standard four-probe technique in zero field with a Linear Research LR-700 AC resistance bridge ($f = 16$ Hz, $I = 1$–3 mA) in the QD MPMS system. Samples were cut and polished into bars with ~1.7 mm lengths and ~0.3×0.3 mm^2 cross section. Four thin platinum wires were attached to the bars with Epo-tek H20E silver epoxy. The current was along the [110] direction.

Temperature-dependent heat capacities were measured in a QD Physical Properties Measurement System using the relaxation technique in zero field for representative samples.

The band structure calculations were performed using a tight-binding linear-muffin-tin orbital method with the atomic-sphere approximation[20,21] using the STUTTGART TB-LMTO program. The experimental lattice parameters and atomic positions were used in the calculations.

III. EXPERIMENTAL RESULTS AND DISCUSSION

WDS measurements were performed on carefully polished (111) surfaces. To exclude the possibility that there is concentration variation along the [111] direction, one sample with nominal concentration 0.02 was picked and the (100) surface was polished. A line scan was made along this surface. All the WDS measurements are summarized in Table I. The line scan result is labeled with an asterisk. N is the number of spots we measured; x_{nominal} is the nominal Al concentration we put in the growth solution; x_{WDS} is the average of WDS measured values for each sample; The error bar is taken as twice the standard deviation σ. We can see that the ratio of x_{WDS} over x_{nominal} is approximately 2.4 for both series. For the batch with $x_{\mathrm{nominal}} = 0.02$ in the $GdFe_2(Al_xZn_{1-x})_{20}$ series, the piece with the (111) surface measured gives x_{WDS} as 0.049 and 2σ as 0.01, and the other piece with the (100) surface measured gives the same x_{WDS} and 2σ values. This suggests that the samples are homogeneous and there is little concentration variation

TABLE I. The WDS data for $GdFe_2(Al_xZn_{1-x})_{20}$ and $YFe_2(Al_xZn_{1-x})_{20}$. N is the number of locations measured in one batch, x_{nominal} is the nominal concentration, x_{WDS} is the average x value measured in one batch, and 2σ is two times the standard deviation of the N values measured. *: This measurement is a line scan along the (100) surface.

$GdFe_2(Al_xZn_{1-x})_{20}$							
N	10	9	9	34	183*	9	9
x_{nominal}	0.0025	0.0050	0.0075	0.02	0.02	0.03	0.05
x_{WDS}	0.005	0.010	0.017	0.049	0.049	0.067	0.122
2σ	0.001	0.001	0.001	0.001	0.001	0.001	0.002

$YFe_2(Al_xZn_{1-x})_{20}$						
N	5	5	5	5	5	5
x_{nominal}	0.0025	0.0050	0.0075	0.01	0.02	0.05
x_{WDS}	0.006	0.009	0.017	0.021	0.047	0.121
2σ	0.000	0.001	0.001	0.001	0.001	0.002

TABLE II. Atomic coordinates and refined site occupancies from single-crystal x-ray measurements for $x_{WDS} = 0.017$ Al-doped $GdFe_2Zn_{20}$ compounds. Agreement factor $R_1 = \Sigma||F_o| - |F_c||/\Sigma|F_o|$.

$x_{WDS} = 0.017$					$R_1 = 0.059$
Atom	Site	x	y	z	Occupancy
Gd	8*a*	0.125	0.125	0.125	1
Fe	16*d*	0.5	0.5	0.5	1
Zn1	96*g*	0.0588(1)	0.0588(1)	0.3265(1)	1
Zn2/Al	48*f*	0.4890(2)	0.125	0.125	0.95(2)/0.05(2)
Zn3	16*c*	0	0	0	1

along any direction; the error bar more likely comes from the machine error rather than the intrinsic sample concentration variation. In the following, the measured, x_{WDS}, rather than nominal x values will be used.

A single-crystal x-ray diffraction measurement was made on the $x_{WDS} = 0.017$ Al-doped $GdFe_2Zn_{20}$ batch and is summarized in Table II. The site refinement has been performed on the single-crystal x-ray data. It reveals that the Zn2 (48*f*) site is the only electron-deficient crystallographic site, i.e., 96*g* and 16*c* are fully occupied. This result in combination with the evidence of WDS reveals that the lighter aluminum is in the crystal and can only be on this specific site. Our experimental data refine very well assuming mixed occupancy of Al and Zn on 48*f*, giving the agreement factor $R_1 = 0.059$. In the $x_{WDS} = 0.017$ Al-doped $GdFe_2Zn_{20}$ sample, Al appears to selectively occupy the Zn2 site with around 5% of Zn2 sites being substituted, which leads to $Al/(Al + Zn) = 0.015$ and is consistent with the WDS measured value within the uncertainties of the two measurements.

Figure 2 shows the evolution of the lattice parameter with x for the $GdFe_2(Al_xZn_{1-x})_{20}$ and $YFe_2(Al_xZn_{1-x})_{20}$ series. We can see that a decreases monotonically with increasing Al doping, which is consistent with Vegard's law and the fact that the Al has a smaller ionic radius than the Zn ion. The inset shows the measured x value vs the nominal x value; in the doping range we studied, similar $x_{nominal}$

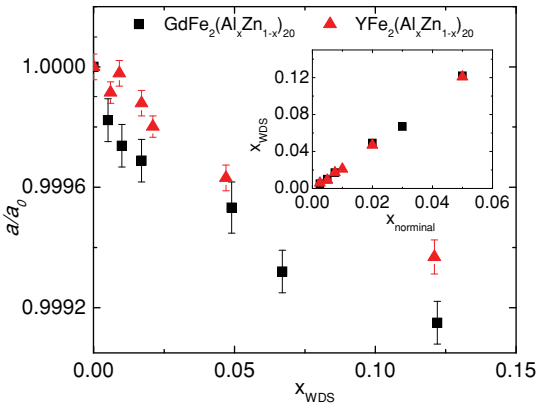

FIG. 2. (Color online) Normalized lattice parameters measured at ~300 K. For the $GdFe_2(Al_xZn_{1-x})_{20}$ series, $a_0 = 14.120$ Å. For the $YFe_2(Al_xZn_{1-x})_{20}$ series, $a_0 = 14.097$ Å. Inset: x_{WDS} vs $x_{nominal}$.

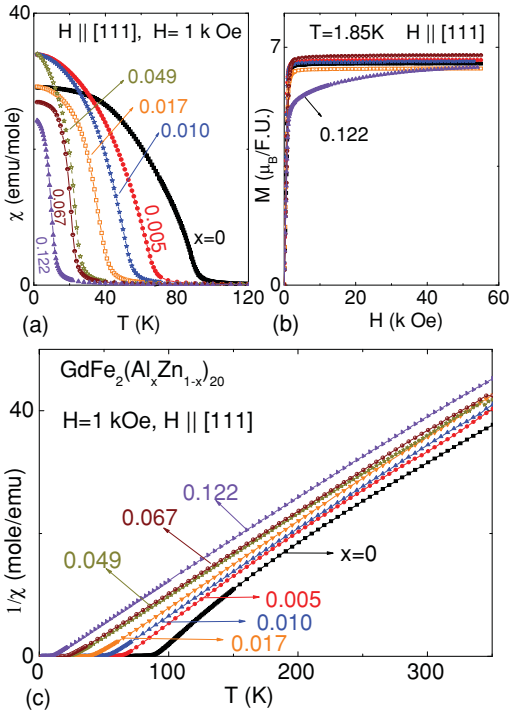

FIG. 3. (Color online) (a) Temperature-dependent magnetic susceptibility data for $GdFe_2(Al_xZn_{1-x})_{20}$ taken at 1 kOe with H along the [111] direction. (b) Field-dependent magnetization data for $GdFe_2(Al_xZn_{1-x})_{20}$ taken at 1.85 K with H along the [111] direction. (c) Temperature-dependent H/M data for $GdFe_2(Al_xZn_{1-x})_{20}$.

resulted in similar x_{WDS} in both $GdFe_2(Al_xZn_{1-x})_{20}$ and $YFe_2(Al_xZn_{1-x})_{20}$ series and the ratio $x_{WDS}/x_{nominal} \sim 2.4$.

Figure 3(a) shows the temperature dependent susceptibility, from 1.85 to 120 K, in an external field $H = 1$ kOe along the [111] direction for $GdFe_2(Al_xZn_{1-x})_{20}$. From the right to the left, x is equal to 0, 0.005, 0.010, 0.017, 0.049, 0.067, and 0.122, respectively. Figure 3(a) shows remarkable similarity with the results for the $Gd(Fe_{1-x}Co_x)_2Zn_{20}$ series.[3] Although we cannot directly infer a precise value for the ordering temperature T_c from $M(T)$ plots, it can still be seen that $GdFe_2(Al_xZn_{1-x})_{20}$ ($x \leqslant 0.122$) shows typical ferromagnetic ordering behavior and T_c decreases with increasing Al doping. Figure 3(b) presents the M vs H data taken at 1.85 K with H parallel to the [111] direction, which rapidly saturate close to but below $7\mu_B$/Gd as the magnetic field increases, consistent with the ferromagnetic ordering in these compounds. Figure 3(c) shows the H/M data from 1.85 to 350 K with applied field 1 kOe along the [111] direction for $GdFe_2(Al_xZn_{1-x})_{20}$. All of these compounds show Curie-Weiss behavior, $1/\chi = (T - \theta_c)/C$, where θ_c is the Curie-Weiss temperature and C is the Curie constant, at high temperature. For $x = 0$, between 200 and 350 K, the fitting results in a μ_{eff} of $8\mu_B$/Gd, which is very close to the theoretical value, $7.94\mu_B$/Gd. However, there is some evident deviation from the Curie-Weiss law below 200 K. For $x = 0$, this feature is most obvious and it can still be seen clearly in the $x = 0.005$ compound, but can only be barely observed in the $x = 0.010$ compound and finally disappears in the $x \geqslant 0.017$ compounds. In the $Gd(Fe_{1-x}Co_x)_2Zn_{20}$ series, this

TABLE III. Summarized $\mu_{\rm eff}$, θ_c, and T_c data from magnetization, heat capacity, and resistivity measurements for $GdFe_2(Al_xZn_{1-x})_{20}$. T_c inferred from the Arrot plot for $x = 0$ is from Ref. 9.

$GdFe_2(Al_xZn_{1-x})_{20}$							
x	0	0.005	0.010	0.017	0.049	0.067	0.122
$\mu_{\rm eff}$ (μ_B)	8	7.8	7.7	7.6	7.8	7.8	7.7
θ_c (K)	51	52	46	43	25	23	3
T_C(mag) (K)[a]	88	63.5	50.5	37.5	22	20.5	9.5
$T_C(\rho)$ (K)[b]	83	63	49	37.5	21.5	20	9
$T_C(C_p)$ (K)[c]	83	63	50	37	22	20.5	9.5

[a] T_c inferred from Arrot plot.
[b] T_c inferred from $d\rho/dT$.
[c] T_c inferred from C_p (see text).

deviation disappears at the $x = 0.12$ doping level.[9] Therefore, for $0.010 \geqslant x \geqslant 0$, the fitting was performed from 350 to 200 K. For all the other concentrations, the fitting was performed from 350 K to the lowest temperature which shows linear behavior in Fig. 3(c). These $\mu_{\rm eff}$ and θ_c are summarized in Table III. All extracted values of $\mu_{\rm eff}$ are close to the theoretical value, varying between $7.6\mu_B$/Gd and $8\mu_B$/Gd. The fact that all θ_c values are positive indicates that ferromagnetic interactions are dominant.

To obtain the T_c values from magnetization measurements, we consider the Arrot-Noakes[22] equation $(H/M)^{1/\gamma} = (M/M_1)^{1/\beta} + (T - T_C)/T_C$, where M_1 is a compound-related constant. In mean-field theory (MFT), $\gamma = 1$, $\beta = 0.5$; therefore H/M is equal to $(M/M_1)^2$ when $T = T_C$; in non-MFT, $\gamma = 4/3$, $\beta = 0.4$;[22] therefore $(H/M)^{3/4}$ is equal to $(M/M_1)^{2.5}$ when $T = T_C$. Within this model, an Arrot plot can be used to infer the ferromagnetic ordering temperature from the magnetization data by noting the temperature at which the low-field data pass through the origin. In order to reduce the uncertainty caused by demagnetization effects, the samples were cut into thin rods whose long axis is along the [111] direction and H was applied along this direction. Figure 4 shows Arrot plots for $x = 0.005$, 0.010, 0.017, 0.049, 0.067, and 0.122. The Arrot plot for pure $GdFe_2Zn_{20}$ can be found in Ref. 9. T_c values obtained from Arrot plots are summarized in Table III. For $x = 0.005$, 0.010, and 0.017, $\gamma = 1$, $\beta = 0.5$ were used. The plots show linear isotherms, and the estimated T_c is 63.5 K for $x = 0.005$, 50.5 K for $x = 0.010$, and 37.5 K for $x = 0.017$. For $x \geqslant 0.049$, the Arrot plots with $\gamma = 1$, $\beta = 0.5$ are no longer perfectly linear, which was also observed in $GdOs_2Zn_{20}$;[9] therefore, the non-MFT values $\gamma = 4/3$, $\beta = 0.4$ are employed for $x \geqslant 0.049$. We can estimate the T_c as 22 K for $x = 0.049$, 20.5 K for $x = 0.067$, and 9.5 K for $x = 0.122$.

For the $GdFe_2(Al_xZn_{1-x})_{20}$ series, the resistivity at 1.85 K ranges from 9 $\mu\Omega$ cm for $x = 0$ to 50 $\mu\Omega$ cm for $x = 0.122$. The residual resistance ratio decreases from 9 for $x = 0$ to 2 for $x = 0.122$. The temperature-dependent resistivity of $GdFe_2(Al_{0.01}Zn_{0.99})_{20}$ is plotted in the inset of Fig. 5 as an example. The resistivity decreases as the temperature decreases and manifests a kink which is caused by the loss of spin disorder scattering. The derivative of the resistivity is used to infer T_c and presented in Fig. 5. Each subsequent data set is shifted downward by 1×10^{-7} $\mu\Omega$ cm/K for clarity and

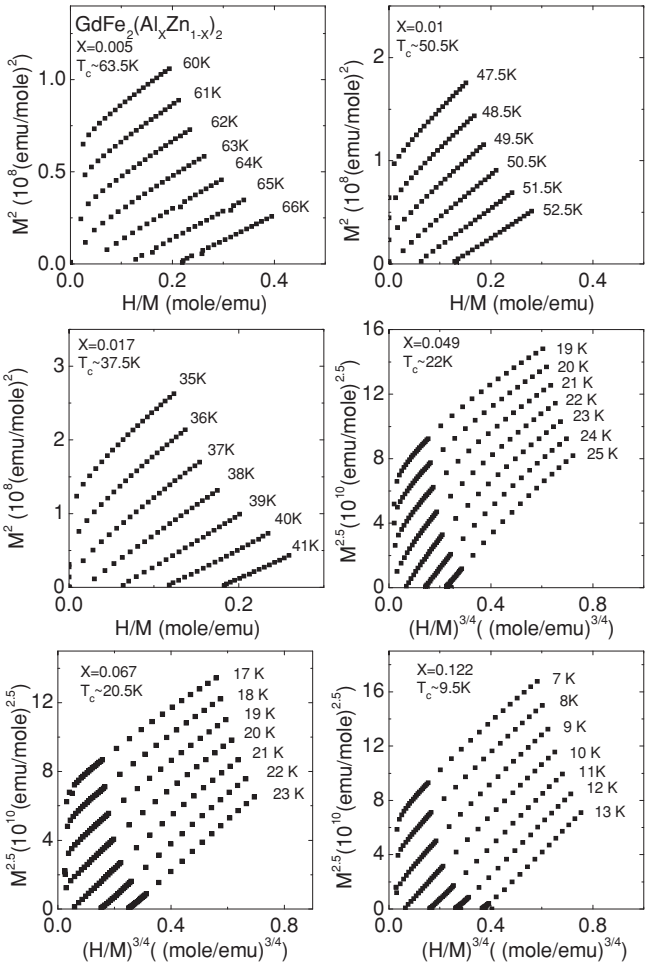

FIG. 4. Isotherms of M^2 vs H/M for the $GdFe_2(Al_xZn_{1-x})_{20}$ series. The temperature at which each measurement was taken is labeled.

the criterion used to infer T_c is shown. The inferred T_c from resistivity data is also summarized in Table III. It can be clearly seen that with Al doping, T_c is suppressed monotonically.

Temperature-dependent specific heat data for the $GdFe_2(Al_xZn_{1-x})_{20}$ series are presented in Fig. 6(a). For samples with $x = 0$, 0.005, 0.010, and 0.017, C_p shows a broad peak near the ferromagnetic phase transition temperature, but for samples with $x = 0.049$, 0.067, and 0.122, as shown in the inset of Fig. 6(a), this feature sharpens. Since $C_p = C_e + C_{ph} + C_M$, where C_e is the conduction electron contribution, C_{ph} is the phonon contribution, and C_M is the local moment contribution, $C_M = C_p - (C_{ph} + C_e)$, where, for $x \leqslant 0.017$, the term in parentheses can be approximated by the C_p data for $LuFe_2Zn_{20}$ since it has a similar molar mass to $GdFe_2Zn_{20}$; for larger x ($x \geqslant 0.049$), the term is better approximated by the heat capacity of YFe_2Zn_{20}. Even with this consideration, a nonrealistic, negative C_M still exists at high temperatures for the $x = 0.122$ sample. The C_M data extracted from this analysis are shown in Fig. 6(b) where the arrows indicate the positions of T_c inferred from the Arrot plot. We clearly see that the magnetic phase transition shows a broad feature in C_M for $0.017 \geqslant x \geqslant 0$: a subtle low-temperature maximum followed by a sharp high-temperature shoulder. As

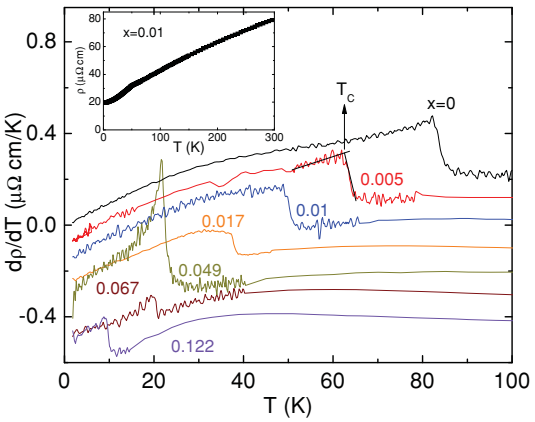

FIG. 5. (Color online) Derivative of the resistivity for the $GdFe_2(Al_xZn_{1-x})_{20}$ series. The arrow shows the criterion used to infer critical temperature. Each subsequent data set is shifted downward by 1×10^{-7} $\mu\Omega$ cm/K for clarity. Inset: Resistivity of $GdFe_2(Al_xZn_{1-x})_{20}$ from 1.85 to 300 K.

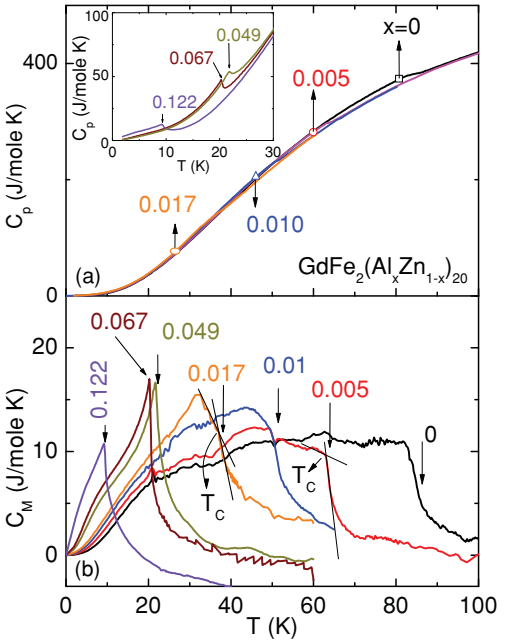

FIG. 6. (Color online) (a) C_p vs T for $x = 0$, 0.005, 0.010, and 0.017 Al-doped $GdFe_2(Al_xZn_{1-x})_{20}$ series. Inset: C_p vs T for $x = 0.047$, 0.069, and 0.122 Al-doped $GdFe_2(Al_xZn_{1-x})_{20}$ series. (b) C_M vs T for $GdFe_2(Al_xZn_{1-x})_{20}$ series. Arrows indicate T_c values determined from the Arrot plot. Thin solid lines on $x = 0.005$ and 0.017 data sets show criteria used to infer T_c.

x increases, the maximum becomes clearer and obviously separates from the sharp high-temperature shoulder. These features can be best seen in the $x = 0.017$ sample, whose C_M contains a clear local maximum around 32 K and a sharp higher-temperature shoulder around 37 K, a value which is more consistent with the $T_C = 37.5$ K inferred from resistivity and magnetization for $x = 0.017$. Thus for the $0.017 \geqslant x \geqslant 0$ samples the temperature of the high-temperature shoulder [shown as the intersection of lines in Fig. 6(b)] is inferred from the C_M data by taking the temperature of the sharp local maximum. A similarly broad feature in C_M was also observed for the $Gd_xY_{1-x}Fe_2Zn_{20}$ ($1 \geqslant x \geqslant 0.02$) series.[8] For higher doping levels, $0.122 \geqslant x \geqslant 0.049$, the magnetic phase transition manifests itself as a sharp peak with T_c right at the position of the maximum of the peak. These T_c values determined from heat capacity data are also presented in Table III.

Table III summarizes the thermodynamic and transport measurements; all values of T_c are consistent with each other, generally giving critical temperatures within ± 1 K of each other. We can see that for the $GdFe_2(Al_xZn_{1-x})_{20}$ series, the ferromagnetic phase transition temperature is suppressed monotonically with Al doping: the transition temperature quickly decreases to 37 K with only 1.7% Al doping, and then more slowly reduces to 22 K with 4.9% Al doping, and 10 K with 12.2% Al doping.

To better understand the systematic changes in Al-doped $GdFe_2Zn_{20}$, the nonmagnetic, isostructural, Al-doped YFe_2Zn_{20} series was grown and characterized. Figure 7(a) shows the temperature-dependent $\Delta M/\Delta H$ of $YFe_2(Al_xZn_{1-x})_{20}$ compounds taken from 2 to 300 K with magnetic field along the [111] direction. Pure YFe_2Zn_{20} is a nearly ferromagnetic Fermi liquid.[3] The susceptibility increases with decreasing temperature, manifesting enhanced paramagnetism behavior; $\Delta M(2\text{ K})/\Delta H$ is around 5.8×10^{-3} emu/mol. With Al doping, the susceptibility is reduced monotonically. At 0.6% and 0.9% Al doping, the susceptibility is still highly temperature dependent with $\Delta M(2\text{ K})/\Delta H$ around 3.2×10^{-3} and 2×10^{-3} emu/mol, respectively while at higher Al doping levels, the susceptibility is roughly temperature independent. Figure 7(b) presents C_p/T vs T^2 data for members of the $YFe_2(Al_xZn_{1-x})_{20}$ series. Since $C_p = C_e + C_{ph}$ in nonmagnetic compounds, which can be approximated as $\gamma T + \beta T^2$ at low temperature, the Sommerfield coefficient, a measure of the density of states at the Fermi level, can be estimated. For pure YFe_2Zn_{20}, γ is 53 mJ/mol K^2; with Al doping, γ is reduced monotonically to 28 mJ/mol K^2 with 1.7% Al doping and 21 mJ/mol K^2 with 12.2% Al doping.

Figures 3 and 7 demonstrate a clear relation between the $GdFe_2(Al_xZn_{1-x})_{20}$ and $YFe_2(Al_xZn_{1-x})_{20}$ series. With Al doping, the strongly correlated conduction electrons in the NFFL YFe_2Zn_{20} become less correlated and the abnormally

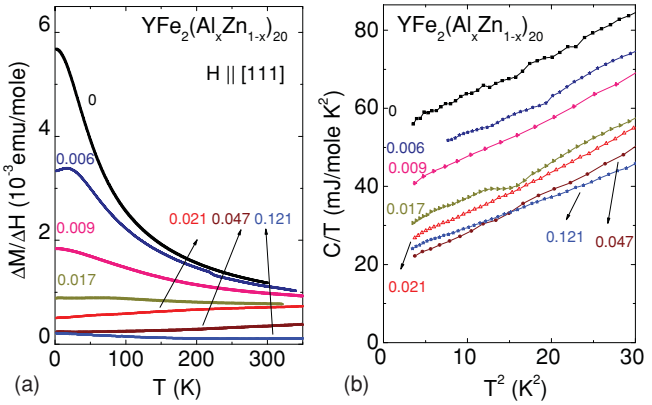

FIG. 7. (Color online) (a) Temperature-dependent $\Delta M/\Delta H$ for $YFe_2(Al_xZn_{1-x})_{20}$ with H parallel to the [111] direction. (b) C_p/T vs T^2 for $YFe_2(Al_xZn_{1-x})_{20}$ series.

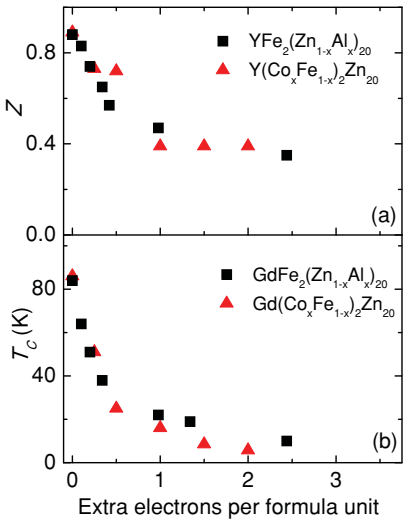

FIG. 8. (Color online) (a) x-dependent Stoner enhancement factor z for Co-doped and Al-doped YFe_2Zn_{20}. (b) x-dependent T_c for Co-doped and Al-doped $GdFe_2Zn_{20}$. The data for Co-doped YFe_2Zn_{20} and $GdFe_2Zn_{20}$ are obtained from Ref. 9.

high ferromagnetic transition temperature (86 K) in pure $GdFe_2Zn_{20}$ is rapidly reduced. The correlation between the $GdFe_2(Al_xZn_{1-x})_{20}$ and $YFe_2(Al_xZn_{1-x})_{20}$ series is very similar to the one between the $Gd(Fe_{1-x}Co_x)_2Zn_{20}$ and $Y(Fe_{1-x}Co_x)_2Zn_{20}$ series:[3] T_c in $GdFe_2Zn_{20}$ and the susceptibility in YFe_2Zn_{20} were reduced monotonically with increased Co doping. The Stoner enhancement factor Z is a measure of the electron correlation (polarizability) and can be expressed as $Z = 1 - (3\mu_B^2)/\pi^2 k_B^2)(\gamma_0/\chi_0) = (1\text{–}1.37) \times 10^{-5}(\gamma_0/\chi_0)$, for χ_0 in units of emu/mol and taken as $\chi(2\text{ K})$ with the core diamagnetism subtracted, and γ_0 in units of mJ/mol K^2. To quantitatively analyze the relation between the polarizability in the Al-doped YFe_2Zn_{20} series and T_c in the Al-doped $GdFe_2Zn_{20}$ series, and compare the effect of Al doping with the effect of Co doping,[3] T_c and Z are plotted (Fig. 8) with the x-axis taken as extra electrons added to the system. The number of extra electrons is calculated as $20x$ per f.u. for Al doping and $2x$ per f.u. for Co doping. Figure 8(a) shows the evolution of the Stoner enhancement factor Z with doping, for Al-doped and Co-doped YFe_2Zn_{20}. Figure 8(b) presents the evolution of T_c with doping for Al-doped and Co-doped $GdFe_2Zn_{20}$. It is worth mentioning that although RFe_2Zn_{20} series are sensitive to the structural disorder,[17] the T_c in the $GdFe_2Zn_{20}$ compound in different batches varies by only ± 3 K,[9] which is around $\pm 3.5\%$ of $GdFe_2Zn_{20}$'s T_c, 86 K.[9] This value is much smaller than the $\sim$15 K difference in T_c for the $TbFe_2Zn_{20}$ compound in different batches.[17] Therefore the monotonic T_c change cannot be due to the structural disorder. There are two features worth noting in this figure. First, the Stoner enhancement factor of $YFe_2(Al_xZn_{1-x})_{20}$ shows a rapid drop when the extra electron counts are smaller than 0.4 per f.u. and then a much slower decrease when more electrons were added. This is very similar to the evolution of T_c with the extra electrons added into $GdFe_2Zn_{20}$ and thus suggests that the high T_c in $GdFe_2Zn_{20}$ is closely related to the polarizability of the conduction electrons. Furthermore, the decrease of polarizability with Al doping also shed some light on the two observations in the $GdFe_2(Al_xZn_{1-x})_{20}$ system: the deviation from the Curie-Weiss law below 200 K for samples with $x \leqslant 0.010$ and the broad C_M peak for samples with $x \leqslant 0.017$. Both unusual behaviors occur in the samples which have apparently larger Z (strong electron correlations), and disappear in the samples which have small Z. This indicates that these behaviors may well be associated with the combination of local moment ordering and the NFFL state. Second, both Al doping and Co doping have very similar effects on the evolution of the Stoner enhancement factor and T_c in this plot. And since the x axis is taken as extra electrons added to the system, the remarkable similarities between Al doping and Co doping support the idea that band filling is important as well as the applicability of a simple rigid-band approximation to these chemically and structurally complicated compounds. Furthermore, the deviation from the Curie-Weiss law below 200 K and the broad C_M peak were also observed for the $Gd(Fe_{1-x}Co_x)_2Zn_{20}$ samples with large Z. This emphasizes the similarities between these two series and reinforces the statement that these two features can be understood as the consequences of Gd^{3+} local moments being embedded in the strongly temperature-dependent, polarizable electronic background of YFe_2Zn_{20}.[9]

Band structural calculations were carried out for YCo_2Zn_{20} and members of the $YFe_2(Al_xZn_{1-x})_{20}$ series ($x = 0$, 0.05, and 0.1). Since the single-crystal x-ray diffraction data show that the Al atoms substitute at Zn2 sites, as shown in Table II, in the band structure calculations, Al atoms were placed solely on the Zn2 sublattice. The calculated total density of states are plotted in Fig. 9 and the Fermi level is indicated by the vertical lines. For pure YFe_2Zn_{20}, the total density of states

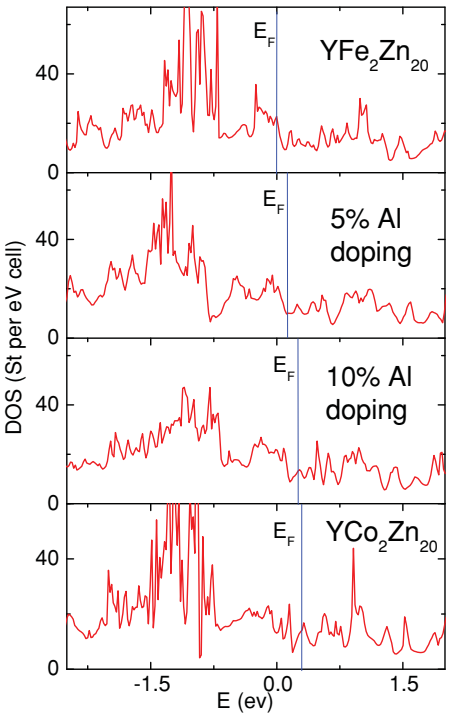

FIG. 9. (Color online) The total density of states (states/eV cell) of YCo_2Zn_{20} and $YFe_2(Al_xZn_{1-x})_{20}$ ($x = 0, 0.05$, and 0.1). The Fermi level is indicated as the vertical line.

at the Fermi level, $D(E_f)$, shows a sharp peak. For Al-doped YFe_2Zn_{20}, the density of states manifests a very similar form to that for pure YFe_2Zn_{20} except the Fermi level shifts to a higher energy level where the density of states drops to a much smaller value, which is comparable to the $D(E_f)$ of YCo_2Zn_{20}. This systematic reduction of the calculated $D(E_f)$ is consistent with the fact that γ decreases with increasing x in the $YFe_2(Al_xZn_{1-x})_{20}$ series. It is worth noting that, with Al doping, $D(E_f)$ first drops rapidly and then enters into a broad valley, which is qualitatively consistent with the nonlinear evolution of T_c and Z. This again gives the theoretically demonstration of the importance of band filling in this system.

IV. CONCLUSION

Single crystals of the $YFe_2(Al_xZn_{1-x})_{20}$ and $GdFe_2(Al_xZn_{1-x})_{20}$ series were grown and characterized by magnetization, heat capacity, and resistivity measurements. T_c in $GdFe_2(Al_xZn_{1-x})_{20}$ and the Stoner enhancement factor in its nonmagnetic analog $YFe_2(Al_xZn_{1-x})_{20}$ series show quantitatively similar evolutions with the extra electrons added in the system: a quick drop first and then a much slower decrease. The comparison with the earlier studies of the $Y(Fe_{1-x}Co_x)_2Zn_{20}$ and $Gd(Fe_{1-x}Co_x)_2Zn_{20}$ series, combined with band structure calculations performed by the tight-binding linear-muffin-tin orbital method with the atomic-sphere approximation, clearly demonstrates the importance of band filling and the applicability of a simple rigid-band approximation to these compounds.

ACKNOWLEDGMENTS

We would like to thank Qisheng Lin and John. D. Corbett for the assistance in powder x-ray measurements. The work at the Ames Laboratory was supported by the Department of Energy, Basic Energy Sciences under Contract No. DE-AC02-07CH11358.

*Present address: Department of Chemistry, Princeton University, Princeton, NJ 08544, USA.

†Present address: Materials Science and Technology Division, Oak Ridge National Laboratory, Oak Ridge, TN 37831, USA.

[1] T. Moriya, *Spin Fluctuations in Itinerant Electron Magnetism* (Springer-Verlag, Berlin, 1985).

[2] T. Nasch, W. Jeitschko, and U. C. Rodewald, Z. Naturforsch. B: Chem. Sci. **52**, 1023 (1997).

[3] S. Jia, S. L. Bud'ko, G. D. Samolyuk, and P. C. Canfield, Nature Phys. **3**, 334 (2007).

[4] M. S. Torikachvili, S. Jia, E. D. Mun, S. T. Hannahs, R. C. Black, W. K. Neils, D. Martien, S. L. Bud'ko, and P. C. Canfield, Proc. Natl. Acad. Sci. USA **104**, 9960 (2007).

[5] P. C. Canfield, S. Jia, E. D. Mun, S. L. Bud'ko, G. D. Samolyuk, and M. S. Torikachvili, Physica B **403**, 844 (2008).

[6] J. S. Kim, G. R. Stewart, and E. D. Bauer, Phys. Rev. B **78**, 035121 (2008).

[7] E. D. Bauer, C. Wang, V. R. Fanelli, J. M. Lawrence, E. A. Goremychkin, N. R. de Souza, F. Ronning, J. D. Thompson, A. V. Silhanek, V. Vildosola, A. M. Lobos, A. A. Aligia, S. Bobev, and J. L. Sarrao, Phys. Rev. B **78**, 115120 (2008).

[8] S. Jia, Ni Ni, S. L. Bud'ko, and P. C. Canfield, Phys. Rev. B **76**, 184410 (2007).

[9] Shuang Jia, Ni Ni, G. D. Samolyuk, A. Safa-Sefat, K. Dennis, Hyunjin Ko, G. J. Miller, S. L. Bud'ko, and P. C. Canfield, Phys. Rev. B **77**, 104408 (2008).

[10] Shuang Jia, Ni Ni, S. L. Bud'ko, and P. C. Canfield, Phys. Rev. B **80**, 104403 (2009).

[11] Yuta Saiga, Kazuyuki Matsubayashi, Masashi Kosaka, Susumu Katano, Masato Hedo, Takehiko Matsumoto, and Yoshiya Uwatoko, J. Phys. Soc. Jpn. **77**, 053710 (2008).

[12] Yuta Saiga, Kazuyuki Matsubayashi, Tetsuya Fujiwara, Takehiko Matsumoto, Masashi Kosaka, Susumu Katano, and Yoshiya Uwatoko, J. Phys.: Conf. Ser. **150**, 042168 (2009).

[13] V. A. Ivanshin, A. A. Sukhanov, D. A. Sokolov, M. C. Aronson, S. Jia, S. L. Bud'ko, and P. C. Canfield, J. Alloys Compd. **480**, 126 (2009).

[14] K. Matsubayashi, Y. Saiga, T. Matsumoto, and Y. Uwatoko, J. Phys.: Conf. Ser. **150**, 042117 (2009).

[15] Yoshiki Nakanishi, Takuya Fujino, Kankichi Ito, Mitsuteru Nakamura, Masahito Yoshizawa, Yuta Saiga, Masashi Kosaka, and Yoshiya Uwatoko, Phys. Rev. B **80**, 184418 (2009).

[16] C. H. Wang, A. D. Christianson, J. M. Lawrence, E. D. Bauer, E. A. Goremychkin, A. I. Kolesnikov, F. Trouw, F. Ronning, J. D. Thompson, M. D. Lumsden, N. Ni, E. D. Mun, S. Jia, P. C. Canfield, Y. Qiu, and J. R. D. Copley, Phys. Rev. B **82**, 184407 (2010).

[17] W. Tian, A. D. Christianson, J. L. Zarestky, S. Jia, S. L. Bud'ko, P. C. Canfield, P. M. B. Piccoli, and A. J. Schultz, Phys. Rev. B **81**, 144409 (2010).

[18] P. C. Canfield and Z. Fisk, Philos. Mag. **65**, 1117 (1992).

[19] T. J. B. Holland and S. A. T. Redfern, Mineral. Mag. **61**, 65 (1997).

[20] O. K. Andersen, Phys. Rev. B **12**, 3060 (1975).

[21] O. K. Andersen and O. Jepsen, Phys. Rev. Lett. **53**, 2571 (1984).

[22] A. Arrot and J. E. Noakes, Phys. Rev. Lett. **19**, 786 (1967).